

Electronic structure of the N-V center in diamond: Experiments

A. Lenef, S. W. Brown, D. A. Redman, and S. C. Rand

Division of Applied Physics, 1049 Randall Laboratory, University of Michigan, Ann Arbor, Michigan 48109-1120

J. Shigley and E. Fritsch

Gemological Institute of America, 1630 Stewart Street, Santa Monica, California 90404-4088

(Received 4 August 1995)

Quantum-beat spectroscopy has been used to observe excited states of the N-V center in diamond. For the 1.945-eV optical transition, direct evidence is presented for the existence of GHz-scale fine structure, together with a much larger 46-cm^{-1} level splitting in the E state. An interference effect observed in transient four-wave-mixing response is explained with a polarization selection rule involving Zeeman coherence among magnetic sublevels. Also, detailed dephasing measurements versus temperature and wavelength have identified the decay mechanisms operative among the various states. A comparison of these results with *ab initio* calculations of excited electronic structure and interactions based on several multielectron models supports the conclusion that the N-V center is a neutral, two-electron center governed by a strong Jahn-Teller effect and weak spin-spin interactions.

I. INTRODUCTION

The center responsible for pink coloration in diamond, a rare tint in natural diamond,¹ but one easily induced in synthetic diamond containing substitutional nitrogen atoms,² is the N-V center. It consists of a nitrogen atom and a vacancy on neighboring sites in the carbon lattice and may be formed through a simple process of irradiation and annealing. While its optical³ and spin-resonance⁴ signatures, as well as its C_{3v} symmetry,⁵ have been known for a long time, the ground-state electronic structure for the center was reassigned only recently, following the observation of unexpected satellite peaks in the persistent hole-burning spectrum.⁶

Recent hole-burning⁷⁻⁹ and electron-paramagnetic-resonance (EPR) experiments¹⁰ have provided firm evidence that the ground state is a spin triplet, rather than a spin singlet as previously thought. The number of active electrons in the center must, therefore, necessarily be even. However, if all unsatisfied bonding electrons in the center are counted (two from nitrogen and three from carbons adjacent to the vacancy), the total is five, which is not even. The existence of triplet levels originally prompted Loubser and van Wyk to suggest⁴ that the center captures an extra electron to form a six-electron center, which is then negatively charged. However, this conclusion runs counter to the stability of the N-V center of temperatures that permit even the heavy nitrogen impurity atoms to become mobile.¹¹ Studies of excess electron centers in alkali halide crystals¹² indicate that they ionize thermally at temperatures well below those necessary to initiate atomic diffusion. A six-electron model would seem unlikely on this basis, and the charge state and physical and electronic structure of the N-V center are called into question.

We believe this puzzling situation is resolved in the present work. Here, we present direct measurements of excited-state energy-level splittings and dynamics, obtained using photon echo spectroscopy, to complement earlier information on magnetic interactions in the ground state.¹³ In a

very direct manner, these measurements permit a determination of electronic excited states and dynamics of the N-V center in the vicinity of the 637-nm zero-phonon transition. The experimental term diagram can then be compared with calculations for centers containing two, four, or six active electrons. Splitting patterns for these three models have been predicted¹⁴ after considering the following electron interactions: spin-orbit, spin-spin, strain, and the Jahn-Teller effect. Consistency between theory and experiment is obtained in the case of two electrons experiencing a Jahn-Teller effect strong enough to quench the spin-orbit interaction,¹⁵ with finer splittings arising from spin-spin interactions.

An important finding is that only two active electrons associated with the nitrogen atom are necessary for understanding the origin of the observed optical transitions of the center. In particular, the dangling bonds on carbons adjacent to the vacancy do not appear to contribute to optical interactions. We are thus led to conclude that the N-V center is a neutral rather than a negatively charged nitrogen-vacancy center, with properties determined by the two active nitrogen electrons.

II. THEORETICAL

The theory of a two- and three-pulse (stimulated) photon echoes has been discussed previously by many authors.¹⁶ In this section, we merely outline the main results and provide extensions of earlier transient four-wave-mixing calculations necessary to understand and analyze our experimental results in a multilevel system with magnetic degeneracy. Of main interest are expressions for photon echo signal intensities versus interpulse delay times for ultrashort pulses, which generate quantum beats and Zeeman coherence described in Sec. II A. When oscillations in the coherence decay are observed as a function of delay between the forward beams (quantum and polarization beats), relatively fine energy-level splittings may be deduced for ground and excited states of the center. When the center wavelength of the incident laser

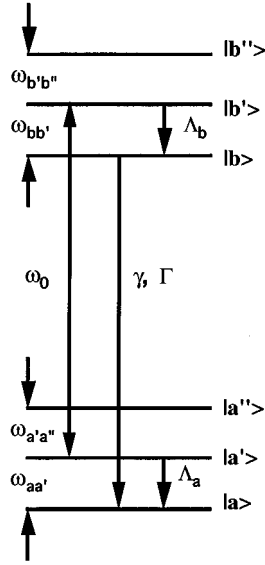


FIG. 1. Schematic energy-level diagram of a luminescent center with quasidegenerate levels a , a' , and a'' in the ground state and b , b' , and b'' in the excited state. Population decay between sublevels is denoted by Λ and between electronic levels by γ . The dephasing rate at the optical resonant frequency ω_0 is Γ .

pulses is tuned over a wide range, for a fixed interpulse spacing, evidence for energy splittings on a coarse scale can also be obtained. In Sec. II B, the parametrization involved in experimental determinations of dephasing mechanisms in this work is examined. Detailed interactions of a center with its surroundings may be deduced when the dephasing rate is measured as a function of temperature over a wide range. We also present explicit expressions for the polarization dependence of echo signals for a center of C_{3v} symmetry in Sec. II C. Polarization studies yield information on magnetic degeneracies.

A. Origin of quantum and polarization beats

Figure 1 depicts energy levels of a luminescent center with ground- and excited-state manifolds a and b , respectively. The manifolds contain sublevels $|a\rangle$, $|a'\rangle$, ... and $|b\rangle$, $|b'\rangle$, ..., which are closely spaced in energy compared to the frequency ω_0 of the optical transition and may be degenerate. The optical frequency between a particular ground-state sublevel $|a\rangle$ and an excited-state sublevel $|b\rangle$ is denoted by $\omega_{ba} = \omega_b - \omega_a$. For simplicity, we assume that population relaxation and dephasing on allowed transitions between excited and ground-state manifolds does not depend on the magnetic substate quantum number. Additionally, intersublevel dephasing and population decay rates are taken to be constant within a given manifold ($\Lambda_{a'a''} = \Lambda_a$ for $a' \neq a''$ and $\Lambda_{b'b''} = \Lambda_b$ for $b' \neq b''$).

The equation of motion for the density matrix ρ describing the interaction of light with a luminescent center is given by¹⁷

$$\dot{\rho} = -\frac{i}{\hbar} [(H_0 + V), \rho] - \left(\frac{\partial \rho}{\partial t} \right)_{\text{relax}}. \quad (1)$$

H_0 is the unperturbed Hamiltonian and V is the light-atom interaction described by

$$V = -e\mathbf{E}(\mathbf{R}, t) \cdot \sum_i \mathbf{r}_i. \quad (2)$$

The electric field \mathbf{E} is evaluated at the position \mathbf{R} of the luminescent center at time t , and \mathbf{r}_i gives the coordinates of the i th electron of the center. The final term in (1) is a relaxation operator with diagonal elements describing population decay and off-diagonal elements describing coherence relaxation (dephasing).

The applied field consists of a sequence of three pulses at times t_j with arbitrary wave vectors \mathbf{k}_j ($j=1, 2$, or 3), of the form

$$\mathbf{E}(\mathbf{R}, t) = \frac{1}{2} \sum_{j=1}^3 \mathbf{e}_j E_j \left(t - t_j - \frac{\mathbf{k}_j \cdot \mathbf{R}}{\omega} \right) \exp\{i[\omega(t - t_j) - \mathbf{k}_j \cdot \mathbf{R} + \phi_j]\} \text{c.c.} +, \quad (3)$$

where \mathbf{e}_j is the polarization vector of the j th field.

In the basis of states shown in Fig. 1, equations of motion for individual density-matrix elements are

$$\dot{\rho}_{b'a'} = (i\omega_{b'a'} + \Gamma)\rho_{b'a'} - \frac{i}{\hbar} \left(\sum_{a''} V_{b'a''} \rho_{a''a'} - \sum_{b''} \rho_{b'b''} V_{b''a'} \right), \quad (4)$$

$$\dot{\rho}_{a'a''} = (i\omega_{a'a''} + \Lambda_{a'a''})\rho_{a'a''} - \frac{i}{\hbar} \sum_{b''} (V_{a'b''} \rho_{b''a''} - \rho_{a'b''} V_{b''a''}) + \delta_{a'a''} \sum_{b''} \gamma \rho_{b''b'}, \quad (5)$$

$$\dot{\rho}_{b''b'} = -(i\omega_{b''b'} + \Lambda_{b''b'})\rho_{b''b'} - \frac{1}{\hbar} \sum_{a''} (V_{b''a''} \rho_{a''b'} - \rho_{b''a''} V_{a''b'}) - \delta_{b''b'} \gamma \rho_{b''b'}, \quad (6)$$

$$\rho_{a'b'} = \rho_{b'a'}^*. \quad (7)$$

Here, γ is the excited-state population decay rate and Γ is the dephasing rate.

To calculate the third-order response associated with three-pulse photon echoes, a third-order perturbation expansion for the density matrix corresponding to a power series in the perturbing field interaction λV is normally developed,

$$\rho = \rho^{(0)} + \lambda \rho^{(1)} + \lambda^2 \rho^{(2)} + \dots. \quad (8)$$

The expansion parameter λ is set equal to one at the end of the calculation. By substituting Eq. (8) into Eq. (1) and equating terms of the same order in λ , a recursion relation may be generated for $\rho^{(n)}$.

$$\dot{\rho}^{(0)} = [H_0, \rho^{(0)}] + L_{\text{relax}} \rho^{(0)}, \quad (9a)$$

$$\dot{\rho}^{(n)} = [H_0, \rho^{(n)}] + V_{\text{relax}} \rho^{(n)} + [V, \rho^{(n-1)}]. \quad (9b)$$

L_{relax} describes linear decay according to $L_{\text{relax}} \rho = -(\delta \rho / \delta t)_{\text{relax}}$ and comprises relaxation, due to spontaneous emission and dephasing by various mechanisms. Assuming that excited-state populations and system coherences are initially zero, one obtains the following equations for system evolution:

$$\dot{\rho}_{b'a'}^{(1)} = -(i\omega_{b'a'} + \Gamma) \rho_{b'a'}^{(1)} + \frac{i}{\hbar} V_{b'a'} \rho_{a'a'}^{(0)}, \quad (10)$$

$$\begin{aligned} \dot{\rho}_{a'a''}^{(2)} = & -(i\omega_{a'a''} + \Lambda_{a'a''}) \rho_{a'a''}^{(2)} + \delta_{a'a''} \sum_{b''} \gamma \rho_{b''b'}^{(2)}, \\ & - \frac{i}{\hbar} \sum_{b''} (V_{a'b''} \rho_{b''a''}^{(1)} - \rho_{a'b''}^{(1)} V_{b''a''}), \end{aligned} \quad (11)$$

$$\begin{aligned} \dot{\rho}_{b''b'}^{(2)} = & -(i\omega_{b''b'} + \Lambda_{b''b'}) \rho_{b''b'}^{(2)} - \delta_{b''b'} \gamma \rho_{b''b'}^{(2)} \\ & - \frac{i}{\hbar} \sum_{a''} (V_{b''a''} \rho_{a''b'}^{(1)} - \rho_{b''a''}^{(1)} V_{a''b'}), \end{aligned} \quad (12)$$

$$\begin{aligned} \dot{\rho}_{b'a'}^{(3)} = & -(i\omega_{b'a'} + \Gamma) \rho_{b'a'}^{(3)} + \frac{i}{\hbar} \left(\sum_{b''} \rho_{b''b''}^{(2)} V_{b''a'} \right. \\ & \left. - \sum_{a''} V_{b'a''} \rho_{a''a'}^{(2)} \right). \end{aligned} \quad (13)$$

In first order, the only nonzero matrix elements correspond to intermanifold coherences. In second order, intramanifold coherence terms and populations appear. Finally, in third order, the off-diagonal term $\rho^{(3)}$ needed to calculate the optical polarization $\mathbf{P} = \text{Tr}(\boldsymbol{\mu}\rho)$ from second-order populations and Zeeman coherences appears.

The evolution of the optical polarization is determined by decay constants of the system and relative timing and polarization of the pulses, together with the pulse areas proportional to the magnitude of the complex field quantities,

$$\tilde{\mathbf{E}}_i = \mathbf{e}_i \exp(-i\mathbf{k}_i \cdot \mathbf{R}) \int_{-\infty}^{\infty} E_i(t) dt. \quad (14)$$

The index i ($=1,2,3$) in (14) labels different input pulses. When the bandwidth of the field greatly exceeds the dephasing rate, the optical pulses can be approximated by δ functions and the equations of motion may be integrated easily. Using the rotating wave approximation, the resulting third-order coherence appropriate for homogeneously broadened media is found to be

$$\begin{aligned} \rho_{b'a'}^{(3)}(t) = & \left(\frac{i}{2\hbar} \right)^3 e^{-\Gamma(t-t_3+t_2-t_1)} e^{-i\omega_{b'a'}(t-t_3)} \sum_{a''b''} \{ \rho_{a''a''}^{(0)} e^{-\Lambda_b(t_3-t_2)} e^{i\omega_{b''b''}(t_3-t_2)} [e^{-i\omega_{b''a''}(t_2-t_1)} (\tilde{\mathbf{E}}_1^* \cdot \boldsymbol{\mu}_{b'a'}) \\ & \times (\tilde{\mathbf{E}}_2 \cdot \boldsymbol{\mu}_{a''b''}) (\tilde{\mathbf{E}}_3^* \cdot \boldsymbol{\mu}_{b''a'}) + e^{i\omega_{b''a''}(t_2-t_1)} (\tilde{\mathbf{E}}_2^* \cdot \boldsymbol{\mu}_{b''a'}) (\tilde{\mathbf{E}}_1 \cdot \boldsymbol{\mu}_{a''b''}) (\tilde{\mathbf{E}}_3^* \cdot \boldsymbol{\mu}_{b''a'})] + e^{(-\Lambda_a + i\omega_{a'a''})(t_3-t_2)} \\ & \times [\rho_{a''a''}^{(0)} e^{i\omega_{b''a''}(t_2-t_1)} (\tilde{\mathbf{E}}_3^* \cdot \boldsymbol{\mu}_{b''a'}) (\tilde{\mathbf{E}}_1 \cdot \boldsymbol{\mu}_{a''b''}) (\tilde{\mathbf{E}}_2^* \cdot \boldsymbol{\mu}_{b''a'}) + \rho_{a'a'}^{(0)} e^{-i\omega_{b''a''}(t_2-t_1)} (\tilde{\mathbf{E}}_3^* \cdot \boldsymbol{\mu}_{b''a'}) (\tilde{\mathbf{E}}_2 \cdot \boldsymbol{\mu}_{a''b''}) \\ & \times (\tilde{\mathbf{E}}_1^* \cdot \boldsymbol{\mu}_{b''a'})] - \rho_{a''a''}^{(0)} (1 - e^{-\gamma(t_3-t_2)}) [e^{-i\omega_{b''a''}(t_2-t_1)} (\tilde{\mathbf{E}}_3^* \cdot \boldsymbol{\mu}_{b''a'}) (\tilde{\mathbf{E}}_2 \cdot \boldsymbol{\mu}_{a''b''}) (\tilde{\mathbf{E}}_1^* \cdot \boldsymbol{\mu}_{b''a'}) + e^{-i\omega_{b''a''}(t_2-t_1)} \\ & \times (\tilde{\mathbf{E}}_3^* \cdot \boldsymbol{\mu}_{b''a'}) (\tilde{\mathbf{E}}_1 \cdot \boldsymbol{\mu}_{a''b''}) (\tilde{\mathbf{E}}_2^* \cdot \boldsymbol{\mu}_{b''a'})] \}. \end{aligned} \quad (15)$$

$\mu_{ab} = e \langle a | \mathbf{r} | b \rangle$ is the usual electric dipole transition moment between states a and b . For inhomogeneously broadened media, only homogeneous groups of centers with positive phase evolution factors $\exp[i\omega_{b''a''}(t_2-t_1)]$ can be rephased by application of the third pulse. These groups generate a macroscopic coherent polarization, which radiates at the echo time $t_{\text{echo}} = t_3 + T$ (where $T = t_2 - t_1$). Only half the terms in (15) contribute at the time of the echo, yielding the polarization

$$\begin{aligned} \rho_{b'a'}^{(3)}(t = t_{\text{echo}}) & = \left(\frac{i}{\hbar} \right)^3 e^{-2\Gamma T} \sum_{a''b''} \rho_{a''a''}^{(0)} e^{i(\omega_{b''a''} - \omega_{b'a'}) T} \\ & \times F_{a'a'';b'b''}(T'), \end{aligned} \quad (16)$$

where $T' = t_3 - t_2$, and

$$\begin{aligned} F_{a'a'';b'b''}(T') & = e^{(-\Lambda_b + i\omega_{b''b''}) T'} (\tilde{\mathbf{E}}_2^* \cdot \boldsymbol{\mu}_{b''a''}) (\tilde{\mathbf{E}}_1 \cdot \boldsymbol{\mu}_{a''b''}) (\tilde{\mathbf{E}}_3^* \cdot \boldsymbol{\mu}_{b''a'}) \\ & + e^{(-\Lambda_a + i\omega_{a'a''}) T'} (\tilde{\mathbf{E}}_3^* \cdot \boldsymbol{\mu}_{b''a''}) (\tilde{\mathbf{E}}_1 \cdot \boldsymbol{\mu}_{a''b''}) (\tilde{\mathbf{E}}_2^* \cdot \boldsymbol{\mu}_{b''a'}) \\ & - (1 - e^{-\gamma T'}) (\tilde{\mathbf{E}}_3^* \cdot \boldsymbol{\mu}_{b''a''}) (\tilde{\mathbf{E}}_1 \cdot \boldsymbol{\mu}_{a''b''}) (\tilde{\mathbf{E}}_2^* \cdot \boldsymbol{\mu}_{b''a''}). \end{aligned}$$

Unless intersublevel dephasing rates Λ_a or Λ_b are exceptionally high, coherence decay is normally determined by the exponential prefactor $\exp(-2\Gamma T)$ in (16), and is twice as fast in inhomogeneous systems as it is in homogeneous systems.

To account for the effect of an inhomogeneous distribution $g(\Delta)$ of resonant frequencies, a spectral average is taken with respect to the detuning $\Delta = \omega_{b_a} - \omega$. Then, the echo polarization is

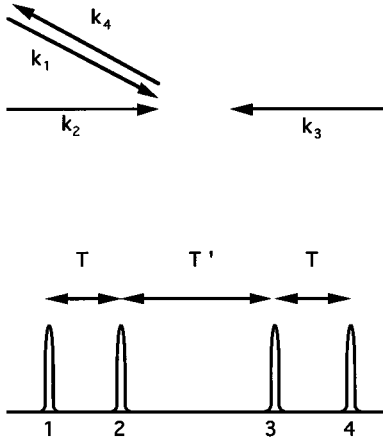


FIG. 2. (a) Diagram of the four-wave-mixing geometry, showing the counter-propagating forward and backward pump beams \mathbf{k}_2 and \mathbf{k}_3 , respectively, and the relative timing between pulses.

$$\begin{aligned}
 \langle \rho_{b'a'}^{(3)}(t') \rangle &= 2\pi \left(\frac{i}{\hbar} \right)^3 e^{-2\Gamma(t'+T)} \sum_{a''b''} \rho_{a''a''}(0) F_{a'a'';b'b''}(T') \\
 &\quad \times \int e^{i(\omega_{b''a''}-\Delta)T} e^{-i(\omega_{b'a'}-\Delta)t'} g(\Delta) d\Delta \\
 &= 2\pi \left(\frac{i}{\hbar} \right)^3 G(t'+\tau) e^{-2\Gamma(t'+T)} \\
 &\quad \times \sum_{a''b''} \rho_{a''a''}(0) F_{a'a'';b'b''}(T') e^{i\omega_{b''a''}T} e^{-i\omega_{b'a'}t'}.
 \end{aligned} \tag{17}$$

Here, we have introduced a convenient time variable $t' = t - t_3$ and $G(t)$ denotes the inverse Fourier transform of $g(\Delta)$.

It is evident from (17) that two kinds of interference can be observed through echo experiments on luminescent centers with discrete levels of the type considered here, depending on whether the delay time T or T' is varied (Fig. 2). If the delay T between the first two pulses is varied, polarization beats occur at frequencies $\Delta\omega = \omega_{b''a''} - \omega_{b'a'}$, which include combinations (sums and differences) of the actual level splittings. These beats arise from interference of polarizations, which do not have a common level. On the other hand, if the delay time T' between pulses two and three is varied, quantum beats occur only at the splitting frequencies $\Delta\omega = \omega_{b''b''}$ and $\Delta\omega = \omega_{a''a'}$ themselves. In this case, the interfering polarizations have a common level.

B. Dephasing mechanisms

Coherence relaxation is determined by radiative and non-radiative processes according to

$$\Gamma_{\text{tot}} = (\gamma_r + \gamma_{\text{nr}})/2, \tag{18}$$

where the radiative contribution is $\gamma_r = \gamma$, and the non radiative portion is given in the case of solids by¹⁵

$$\gamma_{\text{nr}} = a \coth\left(\frac{\hbar\omega_s}{2k_B T}\right) + bT^m + \frac{a\Delta^3}{\exp(\Delta/k_B T) - 1}. \tag{19}$$

The three terms in (19) correspond, respectively, to ‘‘direct’’ one-phonon-assisted decay, indirect two-phonon-assisted Raman decay, and two-phonon Orbach relaxation. The constants a and b weight the different processes and $\hbar\omega_s$ corresponds to the spin state level splitting governing the direct process. Δ gives the energy separation between nearly degenerate spin states and a discrete electronic (or vibrational) state that governs the Orbach process.

From the functional form of (19), it can be recognized that the direct process dominates at low temperatures. At higher temperatures, other decay channels make sizeable contributions. The theoretical exponent for the Raman term is generally taken to be $m=5$,¹⁸ but in this work it was left as an additional fitting parameter to test this theoretical power dependence. Hence, the comparison of (19) with experimental dephasing rates measured versus temperature determines the relative importance of these potential contributions, as well as the three parameters ω_s , Δ , and m .

C. Polarization dependence and Zeeman coherence

Transient four-wave-mixing relies on a tensorial interaction between three incident optical waves and the third-order dipolar response of the system. While most of our experiments were performed with linearly polarized beams, additional information was obtained regarding magnetic properties of the N-V center through observations with circularly polarized beams. Predictions are developed below for Zeeman coherence observable in the N-V center as the result of its electronic-spin character. These calculations show that, in addition to generating quantum beats, interference effects among degenerate magnetic states introduce polarization dependence into photon echo signals.

Ratios of expected photon echo signal intensities for different configurations of incident polarized fields can be calculated from (17) very simply (in the short-time limit $T, T' \rightarrow 0$) by considering the expression for the third-order polarization,

$$P_i^{(3)} = \varepsilon_0 \sum_{jkl} \chi_{ijkl}^{(3)} (\tilde{E}_{1j}^* E_{2k} \tilde{E}_{3l} + \tilde{E}_{1j}^* \tilde{E}_{3k} \tilde{E}_{2l}), \tag{20}$$

and using known or assumed properties of the transition moments comprising the susceptibility:

$$\chi_{ijkl}^{(3)} \propto \frac{1}{n} \sum_{\sigma} \sum_{a', a''} (\mu_{a'b''}^{\sigma})_k (\mu_{b''a''}^{\sigma})_j (\mu_{a''b''}^{\sigma})_i (\mu_{b'a'}^{\sigma})_i. \tag{21}$$

Such a calculation is illustrated in the Appendix, where it is specifically adapted to the N-V center. The notation $(\mu_{ab}^{\sigma})_k$ refers to the k th component of the dipole transition moment between states a and b . The index σ ($\sigma=1\dots n$) in (21) accounts for n possible different defect orientations. Constructive and destructive interferences result from summing the contributions to the third-order response in (20), as described in more detail in the Appendix. Among the possible sequences of circularly polarized pulses, which satisfy momentum conservation, certain ones yield signals an order of magnitude more intense than others. The main predictions are given in Table I.

TABLE I. Comparison of observed and predicted echo properties for various polarization that conserve angular momentum. Only modulation components with relative amplitudes of 15% or more are listed.

Polarization sequence	Theoretical intensity	Observed intensity	Frequencies (GHz)	Relative amplitude
$\sigma^+ \sigma^+ \sigma^+; \sigma^+$	1.0	1.0	0.63 ± 0.01	1.0
			1.63 ± 0.01	0.77
			2.29 ± 0.01	1.29
$\sigma^+ \sigma^+ \sigma^-; \sigma^-$	1.6	0.93	0.56 ± 0.01	1.0
			1.66 ± 0.02	0.37
			2.28 ± 0.01	0.81
			2.88 ± 0.01	0.15
$\sigma^+ \sigma^- \sigma^+; \sigma^-$	0.16	0.11	0.62 ± 0.03	1.0
			1.60 ± 0.02	0.33
			2.27 ± 0.02	0.49
			2.87 ± 0.01	0.23
Linear	1.0	0.93	0.49 ± 0.02	1.0
			1.70 ± 0.01	0.26
			2.29 ± 0.01	0.45
			0.63 ± 0.02	1.0
			1.67 ± 0.02	0.42
			2.30 ± 0.01	0.95
			2.87 ± 0.01	0.23

Signal intensities depend upon details of magnetic degeneracies not immediately evident from the point-group symmetry of the center. Suppression of experimental echoes by an order of magnitude for $\sigma^+ \sigma^- \sigma^+$ polarization sequences compared to $\sigma^+ \sigma^+ \sigma^+$, for example, it is predicted on the basis of Zeeman coherence on $A \leftrightarrow E$ optical transitions of the N-V center, whereas no such effect can occur on $A \leftrightarrow A$ transitions. Hence, observations of interference effects furnish evidence for angular momentum degeneracy and complement more direct methods of assigning the spectroscopic character of states involved in the optical transition.

III. EXPERIMENT

A. Sample preparation

A total of 30 type-1b synthetic single-crystal diamonds of approximate dimensions $1.7 \times 3.5 \times 3.5 \text{ mm}^3$ were obtained from the Sumitomo Electric Corporation for this study. Concentrations of N-V centers in the range $5 \times 10^{16} - 5 \times 10^{18} \text{ cm}^{-3}$ were achieved in these samples using a simple procedure. Infrared-absorption measurements were first used to establish that all as-grown samples contained $200 \pm 20 \text{ ppm}$ substitutional nitrogen atoms, based on the 1130-cm^{-1} calibration.¹⁹ Next, vacancies were created by electron irradiation in a Van de Graaff accelerator. An energy of 1.7 MeV was used for these runs, somewhat above the 0.75-MeV threshold for 1:1 defect creation.²⁰ A current of $20 \mu\text{A}$ was maintained in a beam of diameter 2 cm, delivering a dose rate of $2.4 \times 10^{15} \text{ e}^- \text{ cm}^{-2}/\text{min}$. Irradiation was performed at the triple point of ice, and exposure times varied from 20 min to 50 h. Following irradiation, the samples were placed in a quartz boat and inserted into a furnace filled with argon at $820 \text{ }^\circ\text{C}$ for 4 h. Subsequent to this annealing step, it was noticed that, in addition to turning pink, sample surfaces dulled somewhat due to graphitization, so the large (100)

faces were repolished using traditional methodology²¹ prior to subsequent optical measurements.

Next, the absolute concentration of N-V centers was determined in one sample and related to the magnitude of induced IR absorption at 1332 cm^{-1} (prior to annealing), as well as the irradiation dosage. This was done by first determining the relative density of N-V centers to singly substituted nitrogen from ratios of EPR signals shown in Fig. 3. The main lines at 3300 G correspond to paramagnetic (substitutional) nitrogen and the two sets of four small lines on either side of the nitrogen spectrum correspond to distinguishable orientations of N-V centers. Taking identical oscillator strengths for N and N-V spin transitions, the ratio of integrated intensities for the four low-field N-V lines to the intensity of the central N resonance was found to be 17.5%. Thus, the concentration of centers was $\rho(\text{N-V}) = 0.175\rho(\text{N})$

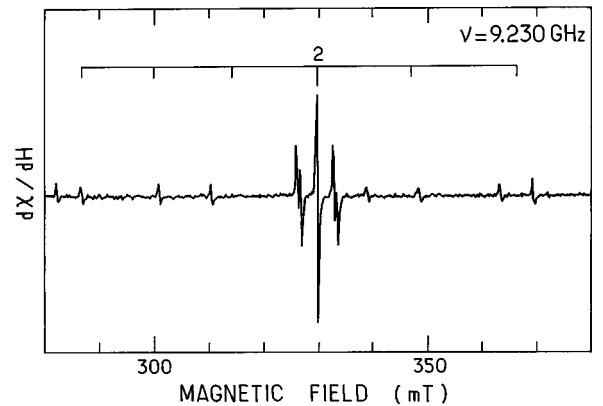


FIG. 3. Electron-paramagnetic-resonance spectra in the region of the isolated nitrogen resonance. The four pairs of small features to the sides are due to four orientationally distinct groups of N-V center. A comparison of line strengths provides the relative concentration of N-V centers to paramagnetic nitrogen (N) directly.

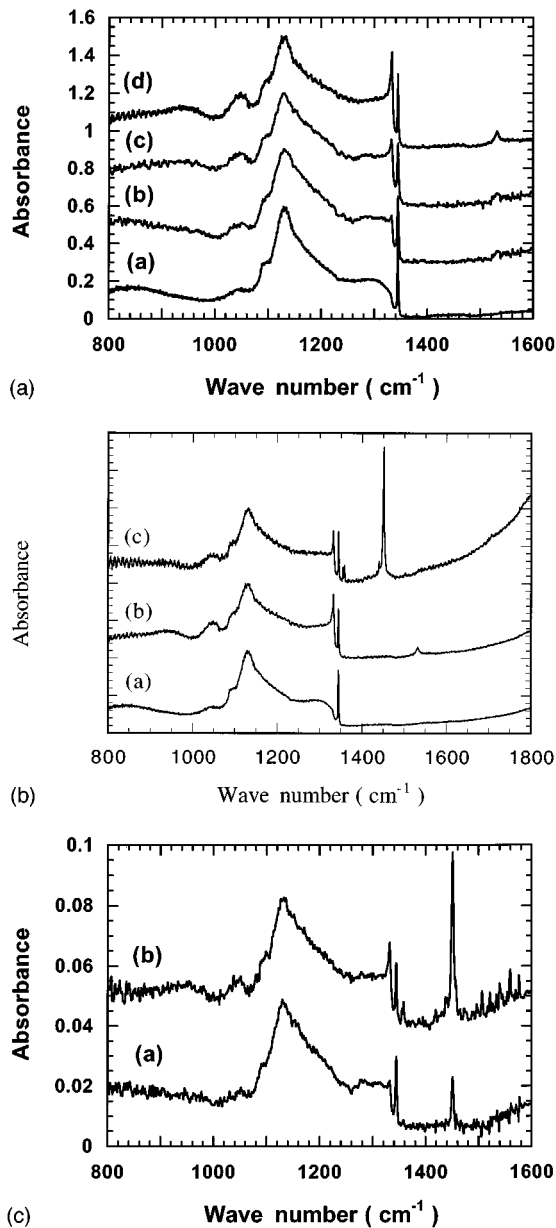


FIG. 4. Infrared-absorption features in synthetic diamond after irradiation. (a) Growth of the 1332-cm^{-1} peak versus 2-MeV electron irradiation dosage. Bottom to top: 0, 1.0×10^{18} , 2.5×10^{18} , and $5 \times 10^{18} \text{ e/cm}^2$. (b) Effects of annealing: reduction of the 1332-cm^{-1} feature and growth of the 1450-cm^{-1} peak. Bottom to top: as grown, after irradiation ($5 \times 10^{18} \text{ e/cm}^2$) and after annealing. Sample thickness was 1.67 mm throughout.

for an electron dose of $1.0 \times 10^{18} \text{ cm}^{-2}$, where $\rho(N)$ is the post-annealing nitrogen concentration. With $\rho(N) = 200 \text{ ppm}/(1 + 0.175)$, the final concentration of centers was determined to be $\rho(N-V) = 30 \pm 10 \text{ ppm}$ for this sample.

In Fig. 4 spectral changes, which occur in the infrared as the result of irradiation [Fig. 4(a)] and annealing [Fig. 4(b) and 4(c)], are shown. In Fig. 5, the relationship between dosage and absorption by induced features at 1332 cm^{-1} is presented for four samples, which had identical initial nitrogen concentrations (221 ppm), to within our ability to measure.

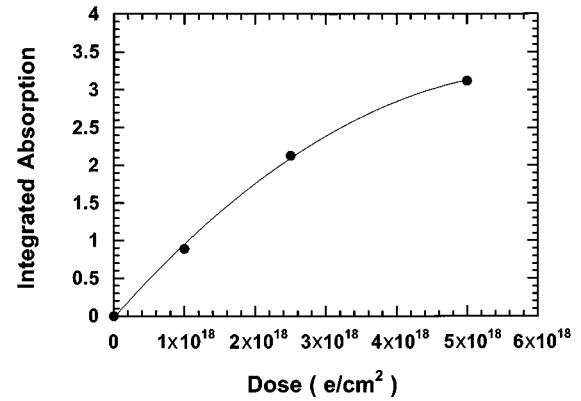


FIG. 5. Dependence of absorbance (integrated between $1330\text{--}1340 \text{ cm}^{-1}$) on electron dosage. The solid curve is a best fit to the regression $y = m_1x + m_2x^2$, with $m_1 = 1.06 \times 10^{-18}$, $m_2 = 8.68 \times 10^{-38}$, after the subtraction of the background ($= 8.3 \text{ cm}^{-1}$) in untreated samples.

B. Four-wave-mixing spectroscopy

Tunable subpicosecond pulses were generated using a synchronously pumped DCM dye laser pumped by a mode-locked 25-W Nd:YAG (yttrium aluminum garnet) laser. An external cavity dumper permitted variable pulse repetition rates from 1 Hz–7.2 MHz. With a conventional output coupler, the laser was capable of generating pulses with autocorrelations yielding full widths at half maximum (FWHM) of 800 fs at a repetition rate of 72 MHz with peak powers of 1–2 kW. Cavity-dumped pulses were in the 10–15-kW range with FWHM autocorrelation widths of 1.02 ps (FWHM Gaussian pulse widths of 700 fs), as determined from second-harmonic generation in a type-I BBO crystal [Fig. 6(a)]. Measured emission spectra were nearly symmetrical Gaussians with a FWHM of 1.0 nm, yielding a time-bandwidth product of 0.4, which is very close to the transform limit [Fig. 6(b)].

Degenerate four-wave mixing was performed in a standard counterpropagating pump geometry (Fig. 7). Most of the measurements were performed on a sample with an absorption-length product somewhat less than unity ($\alpha_0 L < 1$), to ensure linear probe response with maximum signal strength. Transmission was 50% at 637.3 nm in this sample at liquid-helium temperature. When the center wavelength was tuned in the vicinity of 637 nm, a coherent signal beam with an excitation spectrum matching the zero-phonon absorption line of the N-V center was generated in a direction opposite to that of the probe wave. Its intensity was recorded versus temporal delay of the input beams at various temperatures and for various polarizations.

To measure population decay (T_1) in the E state, pulse durations were lengthened to $\tau_p = 5 \text{ ps}$ (autocorrelation FWHM 8 ps) for maximum signal by turning off the saturable absorber jet in the dye laser. The delay between the first two pulses was set to zero and the third pulse delayed by as much as 7 ns, using a double-pass optical delay line [Fig. 7(a)]. Precision alignment of the 60-cm-long, high-resolution mechanical stage used for this purpose was accomplished using a dual-axis silicon position sensor to ensure that the delayed beam remained centered on the interaction region with measured deviations of less than a fiftieth of the focused

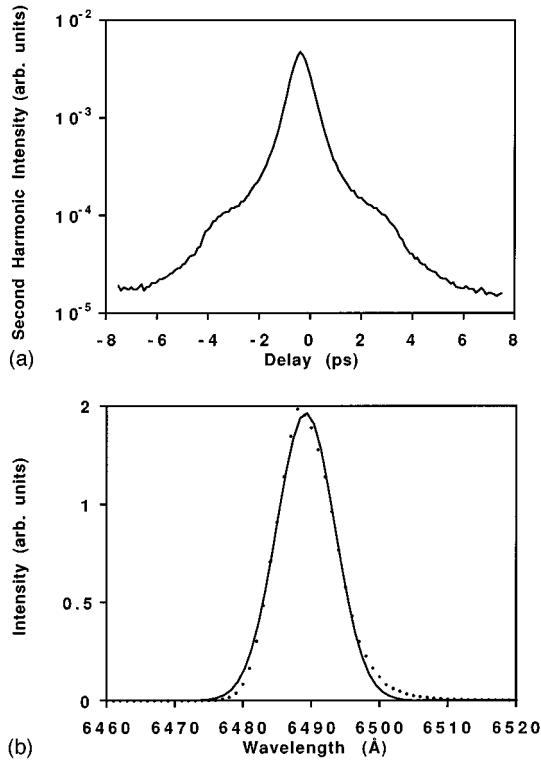


FIG. 6. (a) Second-harmonic autocorrelation of the experimental optical pulses (logarithmic scale) showing a FWHM of 1.02 ps. (b) The optical pulse spectrum corresponding to (a). A Gaussian fit (solid curve) to the data points yields a FWHM of 1.0 nm.

beam diameter over the entire displacement range. The stage was driven by a stepper motor, which typically advanced 3 μm per step. Cavity dumping rates for these measurements were held below 10 kHz to avoid accumulating population in the metastable excited state of the center.¹⁰ This avoided the background signal caused by accumulated gratings, improving the signal-to-noise ratio for observation of weaker single-pulse radiative decays.

The probe intensity was mechanically chopped and synchronous detection applied together with spatial filtering to discriminate against scattered light. Typically 50 scans were averaged. Data were then fitted with single exponential decay functions superimposed on variable background levels.

For T_2 (dephasing) measurements, 1-ps pulses were used and the interval between the second and third pulses was fixed at 1.5 ns, while the delay between the first two pulses was varied [Fig. 7(b)]. Complete decay curves were measured in this way at sixteen temperatures between 5–75 K. The signal magnitude and dephasing time were also measured at fixed interpulse delays, while the excitation wavelength was changed, looking for evidence of coarse excited-state structure. For investigation of polarization selection rules in the four-wave-mixing response, zero-order quarter-wave plates were inserted in the input beams to generate circular polarization. Under these conditions, signals were verified to be circularly polarized and detected through an analyzer consisting of a quarter-wave Babinet-Soleil compensator, linear polarizer, and spatial filter for improved signal isolation.

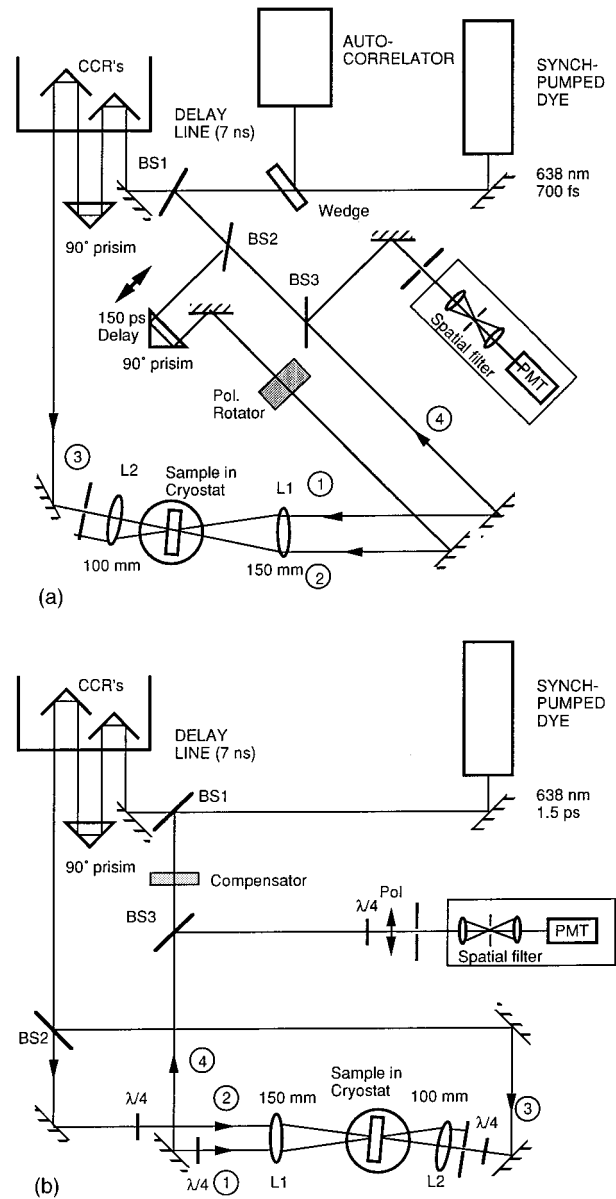


FIG. 7. Setup for (a) T_1 and (b) T_2 measurements.

A study of echo intensity versus cavity-dumping rate was performed to identify the maximum permissible repetition rate, which avoided population accumulation in the metastable level of the N-V center.¹⁰ By varying cavity-dumping rate Q at a constant chopping frequency of 15 Hz, it was found that echo intensity was linear in Q below approximately 10 kHz at liquid-helium temperatures. Hence, all population and dephasing decays were measured at rates lower than this. However, for Q in the MHz range and average input powers of 40–50 mW, the signal beam was visible to the eye. After verifying that quantum beat modulation frequencies did not depend on repetition rate, quantum beat observations were conducted at more elevated rates for better signal-to-noise ratio.

IV. RESULTS AND DISCUSSION

A. Infrared spectroscopy

In this section, changes which occur in the infrared-absorption spectrum of diamond during the formation of N-V

centers are described, inasmuch as they may relate to the excited-state structure of these centers. A strong absorption line appears at 1332 cm^{-1} in proportion to electron irradiation of diamond. Subsequent annealing [Figs. 4(a) and 4(b)] causes single nitrogen impurities to associate with vacancies to form N-V centers, and the strength of this line then diminishes. Simultaneously a sharp feature at 1450 cm^{-1} emerges²² in proportion to dosage and hence (directly or indirectly) to N-V concentration (Fig. 5). This line has previously been attributed to vibrations of a charged nitrogen interstitial,^{23,24} but in view of its appearance during the formation of N-V centers, we briefly discuss the alternative possibility that it is an optical transition of the N-V center itself.

The center responsible for the 1450-cm^{-1} line is known to contain only a single nitrogen atom²³ and exhibits no uniaxial stress splitting along principal directions.²⁵ Since the splitting of orientational degeneracies is too small to be observed by traditional methods, these results and the narrowness of the transition could also be argued to be consistent with absorption to a (metastable) singlet state of an N-V center. No EPR signal has been reported in association with the 1450-cm^{-1} feature.²⁶ This would seem odd if the feature is due to an interstitial, since the impurity is paramagnetic and a shifted resonance might be expected upon displacement of the nitrogen from its substitutional position in the lattice. However, this result has a natural explanation in the case of an N-V model, since these centers have a very weak ground-state EPR signal in the absence of light.¹⁰

The existence of an isotope shift of the 1450-cm^{-1} absorption²³ would seem to favor a vibrational origin of the line. However, the ratio of absorption frequencies for different nitrogen isotopes does not agree very well with the inverse square root of their respective masses, as it should in a straightforward interstitial model. Consequently, the N-V electronic singlet state, the decay signature of which was previously reported by Redman,¹⁰ might profitably be sought by using double-resonance techniques in the region of 180 meV above the ground state.

B. Visible excited-state spectroscopy

1. Population decay

Four-wave-mixing signals were measured versus delay between the second (forward pump) and third (backward pump) pulses at 77 K to obtain the population decay time of the zero-phonon transition. At high repetition rates a strong constant background and appreciable signal intensity were observed at negative delay times. These effects were due to accumulated gratings, as outlined in the previous section. All decay data were, therefore, recorded under conditions such that signal intensities were independent of repetition rate, namely, below 10 kHz at 77 K and below 6 kHz at 6 K.

The decay curve at 637.7 nm is shown in Fig. 8. The data yielded a characteristic time of $\tau=6.48\pm 0.07\text{ ns}$ at 77 K and a derived value of $T_1=2\tau=12.96\pm 0.14\text{ ns}$. The only previously published value of this decay time required instrumental deconvolution,²² but is nevertheless in good agreement with our measurement.

From this radiative decay time, the dipole moment of the $A\rightarrow E$ transition of the N-V center may be estimated,²⁷ yielding $\mu=3.7\times 10^{-27}\text{ cm C}$. In turn, this value permits us to

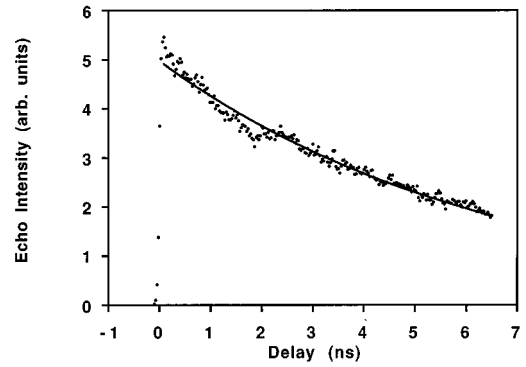


FIG. 8. Excited-state population (T_1) decay of the N-V center obtained with the picosecond resolution at $\lambda=637.2\text{ nm}$ and $T=77\text{ K}$ by varying delay T' . Low signal-to-noise ratio is the result of the need for a low repetition rate to avoid population accumulation in excited states.

estimate a pulse area of $\theta=(\mu E/2\hbar)\tau_p=0.75\text{ rad}$, which confirms that the experiment was performed just within the (perturbative) limit of applicability of theoretical results from Sec. III.

2. Echo modulations

At liquid-helium temperatures, echo dephasing behavior exhibited modulations, the contrast of which depended markedly on the pulse repetition rate. T_2 decay curves of unaccumulated echo signals showed very weak modulation components, whereas accumulated echo signals were nearly 100% modulated. Component frequencies, however, showed no dependence on repetition rate, remaining constant within experimental error over the full range. An example of an accumulated photon echo coherence decay curve is shown in Fig. 9(a).

At negative delays, a small nonzero signal, as well as modulation, is evident in the figure. This signal resulted from free-induction decay, and contributed a (homogeneous) component symmetric about the time origin. It was detected together with the desired photon echo radiation in this experiment, because time-resolved detection was not used for most measurements. However, it was verified that the true photon echo signal accounted for 95% of the four-wave-mixing response at these temperatures in a separate experiment using time-resolved, cross correlation.²⁸

To optimize the Fourier analysis, in the face of rapid decay over a relatively small range, we made use of a Hanning window²⁹ for numerical data processing. The power spectrum shown in Fig. 9(b) for the data of Fig. 9(a) was obtained in this way. A least-squares fitting routine furnished spectral peak positions for the modulation components. At 637.8 nm , strong components were identified at frequencies of $0.63\pm 0.02\text{ GHz}$, $1.600\pm 0.003\text{ GHz}$, $2.298\pm 0.006\text{ GHz}$, and $2.86\pm 0.01\text{ GHz}$. Farther to the red at 638.4 nm , a similar determination yielded frequencies of $0.56\pm 0.01\text{ GHz}$, $1.72\pm 0.01\text{ GHz}$, and $2.290\pm 0.002\text{ GHz}$, showing less than a 10% variation over a detuning range of 1.5 nm from line center.

These values are in excellent agreement with sideband frequencies reported earlier in persistent hole-burning

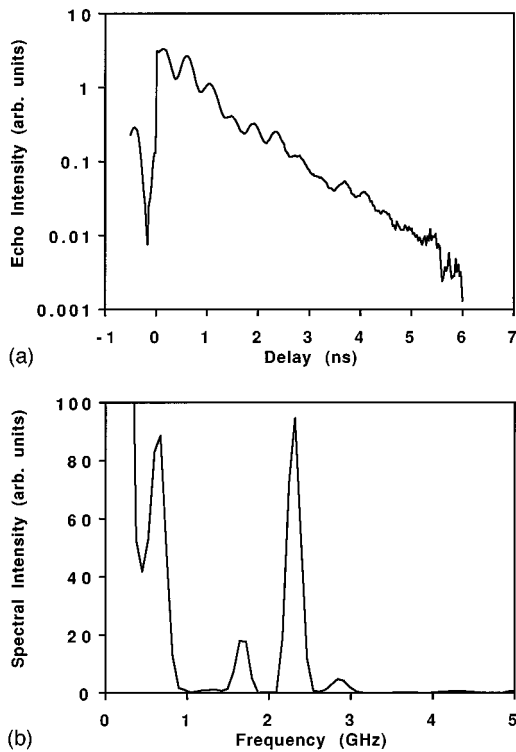


FIG. 9. (a) Modulated echo decay versus delay T at a wavelength of 637.8 nm and a temperature of 6.7 K. All beams were linearly polarized and delay time between pulses two and three was fixed at $T' = 1.5$ ns. (b) Power spectrum of accumulated echo data in (a).

experiments.^{6,9} However, in the present experiments, the interferences responsible for echo modulation were established within the duration of the optical pulses, showing in a direct manner that relaxed excited states are not involved in sideband generation. Consequently, the modulation frequencies can only be related to splittings in the ground or excited states connected directly by the optical field. The presence of a ground-state splitting is directly confirmed by the excellent agreement between the highest-frequency component and the ground-state resonant frequency measured in EPR.^{4,10} Because our measurements were performed by varying the delay between first and second pulses, the observed frequencies should include simple combinations of energy-level splittings, in addition to the pure splittings themselves (see Sec. III). This is the basis for the analysis of the measured frequencies in terms of two excited-state components and their sum frequency in the next section. It provides independent verification of the results and interpretation of hole-burning experiments reported in Ref. 9.

Echo data to the blue side of 637.3 nm, the wavelength at which hole-burning sidebands were reported to become abruptly indistinct in Ref. 9, revealed dramatically increased dephasing rates. This rapid decay unfortunately prevented the use of the Hamming filter to analyze echo data in this spectral range. Consequently, a direct Fourier transform was performed in this region and only a weak component at 2.6 ± 0.05 GHz was identified reliably at an incident wavelength of 635.7 nm. However, this result is once again in accord with persistent hole-burning results. A single homogeneously broadened satellite with this detuning can be seen in pub-

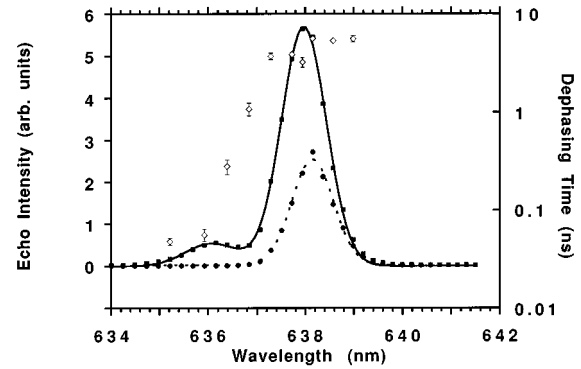


FIG. 10. Echo intensity versus excitation wavelength at 6.1 K. The two curves correspond to different fixed delays of $T=7$ ps (squares) and $T=0.5$ ns (circles). The solid curve is the result of a fit to the sum of two Gaussians with a resultant separation of 46 ± 2 cm^{-1} . Also shown are the dephasing times T_2 measured versus wavelength for $T=7$ ps (diamonds).

lished hole-burning data at $\lambda_{\text{ex}} = 636.699$ nm (Fig. 6 of Ref. 9). This indicates that a change in the electronic structure of the excited state occurs at an energy corresponding roughly to 637.3 nm, an unexpected result which is clarified in the next section.

3. Dephasing mechanisms

Dephasing measurements versus wavelength and temperature revealed different aspects of the electronic structure of the N-V center. The principal results are given in Figs. 10 and 11.

In Fig. 10, the echo intensity recorded at constant delay across the zero-phonon transition clearly resolved itself into two components at different energies, centered around 637 nm. The higher energy component on the blue side of the inhomogeneous distribution of transition wavelengths exhibited very rapid dephasing. The red component dephased ten times more slowly. A least-squares fit to the positions of two

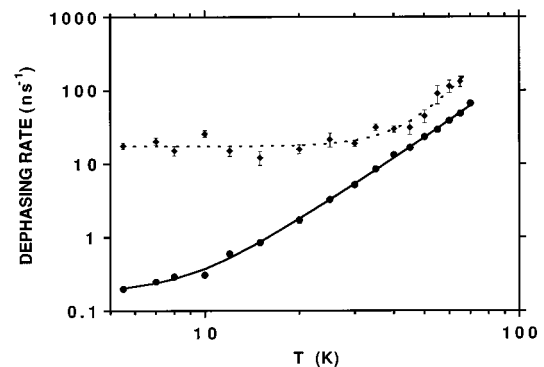


FIG. 11. Temperature dependence of dephasing rate (T_2^{-1}) at wavelengths $\lambda=636.4$ nm (diamonds) and $\lambda=638.4$ nm (circles). The curves give the results of fitting Eq. (18) to the data. For red-detuned data, elimination of Raman or direct dephasing terms resulted in distinctly poorer fits. All contributions were, therefore, included in the final analysis. For blue-detuned data, the Orbach term significantly worsened convergence and did not improve the fit. In this case, it was excluded from the final fit (dashed curve).

TABLE II. Parameters yielding the observed temperature dependence of dephasing.

Wavelength (nm)	a (MHz cm ⁻³)	$\hbar\omega_s/2$ (cm ⁻¹)	Δ (cm ⁻¹)	b (MHz cm ⁻³)	m
638.4	0.1 ± 0.04	10 ± 4	39 ± 5	0.07 ± 0.01	3.2 ± 0.2
636.4	0.06 ± 0.02	68 ± 16		0.04 ± 0.02	5.2 ± 2.6

Gaussian lines yielded a relative splitting of 46 ± 2 cm⁻¹, directly confirming an earlier inference of such an electronic splitting within this line.³⁰ Because the ground-state structure does not admit such a splitting,¹⁰ the excited state itself necessarily consists of two components $|+\rangle$ and $|-\rangle$.

From the results of Fig. 11, it is clear that the mechanism of dephasing also differs on the two sides of the zero-phonon transition. Dephasing rates versus temperature were found to be qualitatively and quantitatively different at representative wavelengths on the red and blue sides of 637 nm, with a sharp transition between them. At 636.4 nm, the dephasing rate was constant below approximately 30 K and increased rapidly above this temperature. At 638.4 nm no plateau was observed and long-wavelength data sustained moderate curvature over the whole temperature range.

Least-squares fits of Eq. (18) to this data yielded the results given in Table II. Dephasing behavior on the blue side of the line was dominated by a direct term with a characteristic energy interval of 68 ± 16 cm⁻¹ below 30 K and a Raman term with $m=5.2 \pm 2.6$ above this temperature. The latter power dependence is characteristic of a non-Kramers center (even number of electrons), in which there are two ($m=7$) or more ($m=5$) excited levels.¹⁸ The Orbach term had to be omitted from the fit for stable convergence, an indication that its degrees of freedom did not contribute to an improved description of the data. Overall, this analysis was consistent with a picture of one-phonon emission between the two components $|+\rangle$ and $|-\rangle$ of the excited state (separated by 46 cm⁻¹) at low temperature and the appearance of an $m=5$ Raman dependence above 30 K.

On the red side of the line, a more complicated parametrization of the temperature dependence emerged from similar analysis. The radiative limit was approached only asymptotically at the lowest temperatures, and between 6–20 K an Orbach term with an energy interval of 39 ± 5 cm⁻¹ made an important contribution. But contributions from a T^m power-law dependence, with $m=3.2 \pm 0.2$ and a direct term with a large energy interval, were not negligible.

Our interpretation of these results is that up to temperatures of 30 K the $|A_1\rangle \leftrightarrow |+\rangle$ optical polarization dephases by a direct $|+\rangle \rightarrow |-\rangle$ decay process, in which a high-frequency phonon is emitted. Above this temperature, a T^5 Raman process sets in. On the other hand, the nonradiative portion of dephasing of the $|A_1\rangle \leftrightarrow |-\rangle$ polarization occurs largely by a two-phonon Orbach process between the $|+\rangle$ and $|-\rangle$ states, at temperatures up to about 20 K. Some centers appear to absorb single phonons to reach the upper excited state $|+\rangle$, whence they make direct radiative transitions to the ground state. At higher temperatures, dephasing is determined by a T^3 process, which was recognized in previous work as indicative of dephasing in a Jahn-Teller (J - T) system with strain energies that are large compared to the couplings be-

tween J - T potential wells.^{15,31} This point is discussed further in the conclusions.

4. Polarization dependence

To obtain information regarding magnetic degeneracies and selection rules for optical transitions of the N-V center, four-wave-mixing experiments were performed with circularly polarized beams, in addition to the measurements with linear polarization. The main results are given in Figs. 12 and 13, and Table I. Figure 12(a) presents a semilogarithmic plot comparing echo intensity versus delay between the first two pulses for two different polarization sequences, namely $(\sigma^+\sigma^+\sigma^+; \sigma^+)$ and $(\sigma^+\sigma^-\sigma^+; \sigma^-)$. Measurements revealed that at 638 nm the overall signal intensity was ten times stronger for the $(\sigma^+\sigma^+\sigma^+; \sigma^+)$ sequence than for the $(\sigma^+\sigma^-\sigma^+; \sigma^-)$ sequence. The ratio of polarized signal intensities did not change much at wavelengths both longer and shorter than 638 nm, and always exceeded one (Fig. 13). Comparative best-fit dephasing times for σ^+ and σ^- signals were $T_2=4\tau_{\text{meas}}=2.78 \pm 0.25$ ns and 2.82 ± 0.09 ns, respec-

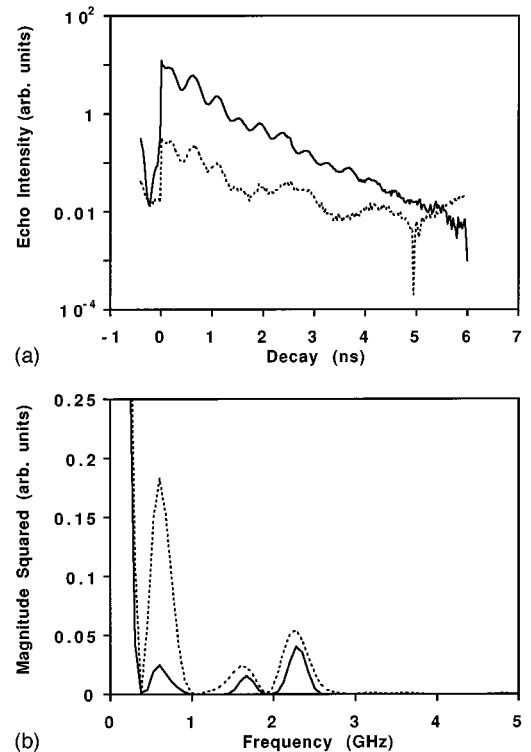


FIG. 12. (a) Logarithmic plots of the polarization dependence of accumulated echo decay curves as a function of T at a fixed value of $T'=1.5$ ns. $\lambda=637.8$ nm and $T=5.5$ K. Polarization sequences are $\sigma^+\sigma^+\sigma^+; \sigma^+$ (solid) and $\sigma^+\sigma^-\sigma^+; \sigma^-$ (dashed). (b) Power spectra of (a).

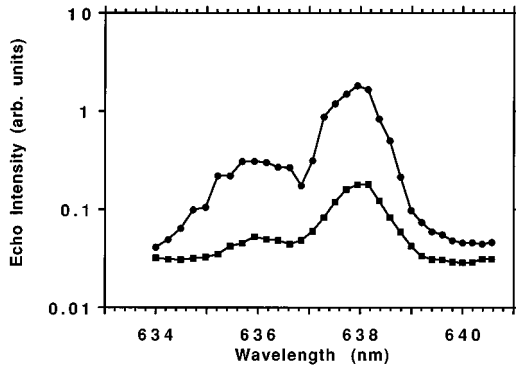


FIG. 13. Echo intensity versus excitation wavelength at 6.1 K for different polarization sequences: $\sigma^+\sigma^+\sigma^+$; σ^+ (circles) and $\sigma^+\sigma^-\sigma^+$; σ^- (squares). Interpulse delays were fixed at $T=0.2$ ns and $T'=1.5$ ns.

tively, on the red side of the zero-phonon line. Modulation components were identical within experimental error, as indicated in Fig. 12(b), except for a slow background modulation at long times believed to be an artifact of acquisition at low signal levels. All results are summarized in Table I.

V. CONCLUSIONS

The variation of four-wave-mixing signal intensity with wavelength clearly revealed the existence of two electronic states $|+\rangle$ and $|-\rangle$ separated by 46 cm^{-1} within the upper state manifold of the 637-nm transition of the N-V center. Modulations at several GHz were detected in time-resolved signals and furnished ground and excited-state spin-spin splittings on a finer frequency scale. Measurements of coherence relaxation rates versus temperature were consistent with $|+\rangle \rightarrow |-\rangle$ decay by one-phonon emission and dephasing in state $|-\rangle$ involved virtual two-phonon (Orbach) excitation of the type $|-\rangle \rightarrow |+\rangle \rightarrow |-\rangle$. At relatively high temperatures, our analysis identified a T^5 Raman decay process in state $|+\rangle$ and a T^3 decay in $|-\rangle$ suggestive of a J - T effect accompanied by strain.

Echo signal variations for different polarization sequences agreed quantitatively with predictions on $A_1, A_2 \leftrightarrow E$ transitions of a C_{3v} center when Zeeman coherence in the spin triplet ground state was taken into account. Suppression of echoes was uniform over an excitation wavelength range that probed different excited states. This indicated that this effect depended on ground-state spin sublevel degeneracy. Moreover, only the first two pulses had a significant overlap within the excited-state dephasing time T_2 . Interference effects with long coherence times could, therefore, only have arisen from Zeeman coherence between ${}^3A(m_s = +1)$ and ${}^3A(m_s = -1)$ ground states. This set of observations confirmed the residual $m_s = \pm 1$ ground-state degeneracy already known from EPR studies,¹⁸ as well as the E orbital angular momentum symmetry of the excited state required to produce echo polarization dependence.

Our overall results are consistent with the excited-state structure sketched in Fig. 14. We believe that neither the coarse-grain excited-state splittings nor the finer GHz splittings are determined by uniaxial strain. Internal strains are ordinarily randomly oriented from sample to sample, as well

as from point to point within any given sample. For a hypothetical sample with a permanent internal, uniaxial strain, one would not expect internal strain to be universally oriented along a unit-cell diagonal in synthetic and natural samples, and it could not be parallel to the threefold axis of more than one of the four distinguishable classes of N-V center in diamond. Hence in the limit of large strain, we point out that irregular, inhomogeneous distributions of N-V center resonance frequencies would be expected in different samples rather than a single well-defined splitting.

The T^3 dephasing behavior of $|-\rangle \leftrightarrow |A\rangle$ dipole polarization at high temperature suggests a different origin for the observed electronic structure, namely, a Jahn-Teller effect accompanied by strain. On the basis of temperature dependence of line positions and widths,³² as well as uniaxial strain measurements,⁵ it was concluded, in previous work, that E vibrational modes couple only weakly to the N-V center and do not produce a significant J - T distortion of the excited state. Mixing of $|+\rangle$ and $|-\rangle$ components of the strain-split line measured by polarized luminescence techniques in this earlier work agreed with proportions expected from random strain, with a magnitude corresponding to the inhomogeneous linewidth. The possibility of J - T coupling was, therefore, dismissed. However, the experimental results presented in the present paper are more consistent with the opposite conclusion. Moderate amounts of random strain alone certainly do not explain our quantum beat results, since a continuous strain distribution would merely broaden the excited state. Well-defined quantum beats would never form.

We propose a model in which $|+\rangle \rightarrow |-\rangle$ coupling arises from a strong Jahn-Teller interaction with a splitting between vibronic levels (46 cm^{-1}), which slightly exceeds the inhomogeneous linewidth (FWHM 25 cm^{-1}). This coupling strength is large enough to quench spin-orbit coupling,³³ so that a $|+\rangle$ and $|-\rangle$ manifold structure augmented by spin-spin splittings can be preserved overall, in apparent agreement with our experiment. This situation would explain why the

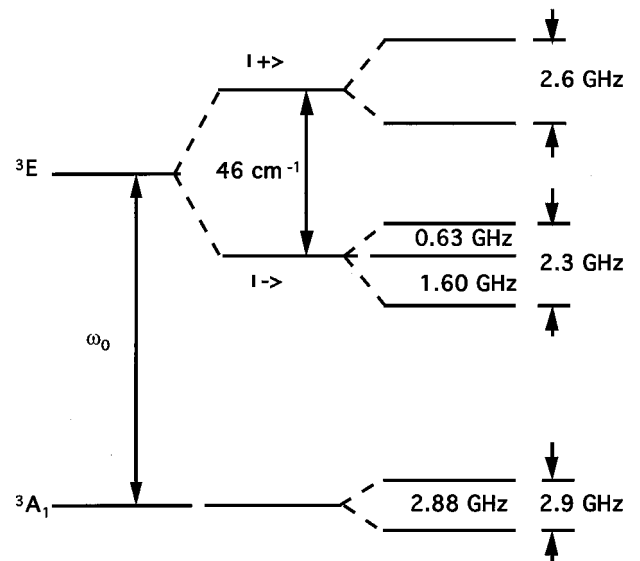


FIG. 14. Empirical energy-level structure deduced for the N-V center from photon echo observations.

Jahn-Teller interaction was not evident in earlier measurements.³³ In our model, strain does not couple magnetic substrates together in first order, so that spin-spin interactions are insensitive to both strong J - T coupling and strain. In the presence of quenching of the spin-orbit interaction, this model can explain why excited and ground-state splittings generate quantum beat frequencies of similar magnitude.

Detailed molecular-orbital calculations presenting the aspects of this model for centers with different assumed numbers of active electrons are presented in Ref. 14. A comparison of these calculations with the present experimental results shows that unless a Jahn-Teller interaction is introduced in the excited E state, the coarse splitting resolved in this work and the existence in the excited state of the three fine rf splittings that we have observed are not satisfactorily explained. Hence, this research supports the conclusion that the N-V center is a neutral, two-electron center governed primarily by a strong Jahn-Teller effect and weak spin-spin interactions.

ACKNOWLEDGMENTS

This research was sponsored in part by the Air Force Office of Scientific Research (H. Schlossberg) and the National Science Foundation Technology Center for Ultrafast Optical Science (STC PHY 8920108). A. Lenef, D. Redman, and S. Brown gratefully acknowledge support from a DSO fellowship from the Department of Education, an AT&T scholarship, and a Rackham Dissertation Grant, respectively. The authors are indebted to L. Haliburton, S. Yazu, S. Satoh, and K. Tsuji of Sumitomo Electric for electron irradiation of samples, and to Carol Stockton for assistance with infrared-absorption spectroscopy. We also wish to thank R. Schwartz and N. Manson for helpful discussions.

APPENDIX

To compare third-order responses to various input pulse polarization sequences for transitions between states of specific orbital angular momentum symmetries, contributions to the third-order polarization $\mathbf{P}^{(3)}$ from all possible transitions need to be considered. In these calculations, it is essential to account for the vector character of the optical field in the scalar interaction of Eq. (2). We outline such calculations below and show, from Eq. (20), for example, that a $\sigma^+ \sigma^+ \sigma^+$ input sequence yields an x component of the four-wave-mixing polarization given by

$$P_x^{(3)} = 2\epsilon_0 E_0 |E_0|^2 (\chi_{xxxx}^{(3)} + \chi_{xxyy}^{(3)} - \chi_{xyxy}^{(3)} + \chi_{xyyx}^{(3)}), \quad (\text{A1})$$

whereas a $\sigma^+ \sigma^- \sigma^+$ input sequence yields

$$P_x^{(3)} = 2\epsilon_0 E_0 |E_0|^2 (\chi_{xxxx}^{(3)} - \chi_{xxyy}^{(3)} - \chi_{xyxy}^{(3)} - \chi_{xyyx}^{(3)}), \quad (\text{A2})$$

which is quite different from (A1). Such differences result in striking changes of echo intensities for different polarization sequences.

For specified initial and final states, the calculation of susceptibility proceeds by writing the dipole matrix elements,

$$\mu_{\alpha\beta} = -e \langle \phi_\alpha | \mathbf{r} | \phi_\beta \rangle, \quad (\text{A3})$$

for each electron of the center in appropriate irreducible representations α and β of orbital angular momentum states $|\phi\rangle$, referenced to the coordinate system of the luminescent center.¹⁴ \mathbf{r} does not act on the spin of the center, so spin matrix elements are not considered. Circularly polarized fields can of course alter spin states, but for the purposes of this discussion it is adequate to set all spin matrix elements to be equal and nonzero. The components of \mathbf{r} transform as X , Y , and Z (defect coordinates), and, therefore, in C_{3v} symmetry can be expressed as $A_1 \oplus E$ operators according to $r^{A_1} = Z$, $r_X^{E_1} = X$ and $r_Y^{E_2} = Y$. Similarly, irreducible forms of the unit vectors in crystal coordinates are $\mathbf{e}^{A_1} = \mathbf{e}_Z$, $\mathbf{e}^E = \mathbf{e}_X$, and $\mathbf{e}^E = \mathbf{e}_Y$.

For Z oriented along a cube diagonal, transformations between defect coordinates (x, y, z) and irreducible crystal coordinates are given by

$$\mathbf{r} = r^{A_1} \mathbf{e}^{A_1} + r_X^E \mathbf{e}_X^E + r_Y^E \mathbf{e}_Y^E, \quad (\text{A4})$$

where

$$\begin{aligned} r^{A_1} &= \frac{1}{\sqrt{3}} (x + y + z), \\ r_X^E &= \frac{1}{\sqrt{6}} (2z - x - y), \\ r_Y^E &= \frac{1}{\sqrt{2}} (x - y), \end{aligned} \quad (\text{A5})$$

and

$$\begin{aligned} \mathbf{e}^{A_1} &= \frac{1}{\sqrt{3}} (\mathbf{e}_x + \mathbf{e}_y + \mathbf{e}_z), \\ \mathbf{e}_X^E &= \frac{1}{\sqrt{3}} (2\mathbf{e}_z - \mathbf{e}_x - \mathbf{e}_y), \\ \mathbf{e}_Y^E &= \frac{1}{\sqrt{3}} (\mathbf{e}_x - \mathbf{e}_y). \end{aligned} \quad (\text{A6})$$

Representations of \mathbf{r} for the other seven (cube diagonal) orientations in crystal coordinates can be found with transformations between octants of a sphere. Then, by applying the Wigner-Eckart theorem, matrix elements between all combinations of irreducible orbital angular momentum states can be found. These are listed below:

$$\langle \phi^{A_1} | \mathbf{r} | \phi^{A_1} \rangle = \mathbf{e}^{A_1} \langle \phi^{A_1} | r^{A_1} | \phi^{A_1} \rangle, \quad (\text{A7})$$

$$\langle \phi^{A_2} | \mathbf{r} | \phi^{A_1} \rangle = 0,$$

$$\langle \phi_X^E | \mathbf{r} | \phi^{A_1} \rangle = \mathbf{e}_X^E \langle \phi^E | r^E | \phi^{A_1} \rangle,$$

$$\langle \phi_Y^E | \mathbf{r} | \phi^{A_1} \rangle = \mathbf{e}_Y^E \langle \phi^E | r^E | \phi^E \rangle,$$

$$\langle \phi^{A_2} | \mathbf{r} | \phi^{A_2} \rangle = \mathbf{e}^{A_1} \langle \phi^{A_2} | r^{A_1} | \phi^{A_2} \rangle,$$

$$\langle \phi_X^E | \mathbf{r} | \phi^{A_2} \rangle = -\mathbf{e}_Y^E \langle \phi^E | r^E | \phi^{A_2} \rangle,$$

$$\langle \phi_Y^E | \mathbf{r} | \phi^{A_1} \rangle = \mathbf{e}_X^E \langle \phi^E | r^E | \phi^{A_2} \rangle,$$

$$\langle \phi_X^E | \mathbf{r} | \phi_X^E \rangle = \mathbf{e}^{A_1} \langle \phi^E | r^{A_1} | \phi^E \rangle + \frac{1}{\sqrt{2}} \mathbf{e}_Y^E \langle \phi^E | r^E | \phi^E \rangle,$$

$$\langle \phi_Y^E | \mathbf{r} | \phi_Y^E \rangle = \frac{1}{\sqrt{2}} \mathbf{e}_X^E \langle \phi^E | r^E | \phi^{A_2} \rangle,$$

$$\langle \phi_Y^E | \mathbf{r} | \phi_Y^E \rangle = \mathbf{e}^{A_1} \langle \phi^E | r^{A_1} | \phi^E \rangle - \frac{1}{\sqrt{2}} \mathbf{e}_Y^E \langle \phi^E | r^E | \phi^E \rangle.$$

The remaining matrix elements may be obtained by taking complex conjugates of the expressions above. The dipole matrix element $\langle \phi^{A_2} | r | \phi^{A_1} \rangle$ is zero, because r transforms as $A_1 \otimes E$ under C_{3v} symmetry. The reduction of the product representation for this matrix element does not contain the totally symmetric representation A_1 .

Application of these results to the echo susceptibility in (21) determines third-order selection rules between any two states of specific symmetry. First of all, the susceptibility tensor exhibits general symmetry relations, which are useful, namely, $\chi_{ijkl}^{(3)} = \chi_{jikl}^{(3)}$ and $\chi_{ijkl}^{(3)} = \chi_{klij}^{(3)}$. Additionally, other simplifications result from specific geometries or configurations, like that of circularly polarized input fields coupling nondegenerate states. For an $A_1 \rightarrow A_1'$ transition, with a transition moment lying along the [111] direction, one finds

$$\begin{aligned} \chi_{xxxx}^{(3)}([111]) &= |\langle \phi^{A_1'} | r^{A_1} | \phi^A \rangle|^2 (\mathbf{e}^{A_1} \cdot \mathbf{e}_x) (\mathbf{e}^{A_1'} \cdot \mathbf{e}_x) (\mathbf{e}^{A_1} \cdot \mathbf{e}_x) \\ &\quad \times (\mathbf{e}^{A_1'} \cdot \mathbf{e}_x) = \frac{1}{9} |\langle \phi^{A_1'} | r^{A_1} | \phi^A \rangle|^2. \end{aligned} \quad (\text{A8})$$

In view of the totally symmetric form of the basis vector $\mathbf{e}^{A_1} = (\mathbf{e}_x + \mathbf{e}_y + \mathbf{e}_z)/\sqrt{3}$, all tensor components of $\chi_{xxxx}^{(3)}([111])$ are equal on an $A_1 \rightarrow A_1'$ transition. Susceptibility contributions from centers oriented along other cube diagonals can be found by coordinate transformations equivalent to reflections in (100), (010), and (001) planes.

Also, because χ_{ijkl} transforms like the outer product $r_i r_j r_k r_l$, components with indices that are repeated an odd number of times change sign when the orientation is reflected in these planes. Consequently, when all eight possibilities for the orientation of N-V centers are taken into account, the total $xxxy$ component of the susceptibility, for example, is given by

$$\begin{aligned} \chi_{xxxx}^{(3)} &= \frac{1}{8} [\chi_{xxxx}^{(3)}([111]) + \chi_{xxxx}^{(3)}([\bar{1}11]) + \chi_{xxxx}^{(3)}([1\bar{1}1]) + \dots \\ &\quad + \chi_{xxxx}^{(3)}([\bar{1}\bar{1}\bar{1}])] = 0. \end{aligned} \quad (\text{A9})$$

Consequently, only χ components in which indices appear an even number of times make nonzero contributions to the total response.

For degenerate states, the signal polarization depends strongly on the polarization sequence of the incident pulses. For example, using (21) to find the susceptibility for an $A_1 \rightarrow E$ transition, one obtains

$$\begin{aligned} \chi_{xxxx}^{(3)} &= C \{ (\mu_{A_1, E_X})_k (\mu_{E_X, A_1})_j (\mu_{A_1, E_X})_l (\mu_{E_X, A_1})_i \\ &\quad + (\mu_{A_1, E_X})_k (\mu_{E_X, A_1})_j (\mu_{A_1, E_Y})_l (\mu_{E_Y, A_1})_i \\ &\quad + (\mu_{A_1, E_Y})_k (\mu_{E_Y, A_1})_j (\mu_{A_1, E_X})_l (\mu_{E_X, A_1})_i \\ &\quad + (\mu_{A_1, E_Y})_k (\mu_{E_Y, A_1})_j (\mu_{A_1, E_Y})_l (\mu_{E_Y, A_1})_i \}. \end{aligned} \quad (\text{A10})$$

The constant C is given by $C = (i/2\hbar)^3 g(0) \rho_{A_1, A_1(0)}$. Evaluation of tensor components with an even number of repeated indices then yields the expressions

$$\begin{aligned} \chi_{xxxx}^{(3)} &= \chi_{yyyy}^{(3)} = \chi_{zzzz}^{(3)} = \chi_{xxyy}^{(3)} = \chi_{yyzz}^{(3)} = \chi_{zzxx}^{(3)} \\ &= \frac{4}{9} C |\langle \phi^E | r^E | \phi^{A_1} \rangle|^4, \end{aligned} \quad (\text{A11})$$

and

$$\chi_{xxyy}^{(3)} = \chi_{yyzz}^{(3)} = \chi_{zzxx}^{(3)} = \frac{1}{9} C |\langle \phi^E | r^E | \phi^{A_1} \rangle|^4. \quad (\text{A12})$$

These values are, in fact, equal to the final susceptibility after averaging over all orientations of a C_{3v} center with a transition moment along a cube diagonal, because transformations between equivalent orientations do not change the signs of susceptibilities which have an even number of repeated indices. Evaluation of the third-order susceptibility for an $E \leftrightarrow E$ transition yields results qualitatively similar to those for $A_1 \leftrightarrow E$, and will not be considered here.

In summary, the susceptibilities for different circularly polarized pulse sequences on $A_1 \leftrightarrow A_1$ or $A_2 \leftrightarrow A_2$ transitions are the same. For instance,

$$P_x^{(3)}(\sigma^+ \sigma^+ \sigma^+; \sigma^+) = P_x^{(3)}(\sigma^+ \sigma^- \sigma^+; \sigma^-), \quad (\text{A13})$$

where the first three σ polarizations in parentheses indicate input fields and the last one indicates the output field. No dependence of the echo intensity is expected for transitions between nondegenerate states. On the other hand, if one state (or both states) of a transition is (are) degenerate within the excitation bandwidth, a strong intensity dependence of echo response is predicted. For an $E \leftrightarrow A_1$ transition, we find

$$P_x^{(3)}(\sigma^+ \sigma^+ \sigma^+; \sigma^+) = \frac{10}{9} \varepsilon_0 C |\langle \phi^E | r^E | \phi^{A_1} \rangle|^4 |E_0| |E_0|^2, \quad (\text{A14})$$

whereas

$$P_x^{(3)}(\sigma^+ \sigma^- \sigma^+; \sigma^-) = -\frac{4}{9} \varepsilon_0 C |\langle \phi^E | r^E | \phi^{A_1} \rangle|^4 |E_0| |E_0|^2. \quad (\text{A15})$$

Results for $E \leftrightarrow A_2$ transitions are similar, with A_1 replaced by A_2 in the reduced matrix element. The intensities predicted on the basis of squaring these signal polarizations $\mathbf{P}^{(3)}$

for the four possible sequences of σ -polarized pulses, which conserve angular momentum, are given in Table I. Polarization dependence of four-wave mixing has been described previously³⁴ for transitions between atomic states of well-

defined total angular momenta. The method and results presented here permit predictions, however, even when no information on quantum numbers is available, but wavefunction symmetries are known.

-
- ¹J. E. Shigley, E. Fritsch, C. M. Stockton, J. I. Koivula, C. W. Fryer, and R. E. Kane, *Gems Gemol.* **22**, 192 (1986).
- ²A. T. Collins, *J. Phys. C* **16**, 2177 (1983); S. C. Rand, in *Tunable Solid State Lasers II*, edited by A. B. Budgor, L. Esterowitz, and L. G. DeShazer (Springer-Verlag, New York, 1986), pp. 276–280.
- ³L. duPreez, Ph.D. dissertation, University of Witwatersrand, 1965.
- ⁴J. H. N. Loubser and J. A. Van Wyk, *Diamond Research* (Industrial Diamond Information Bureau, London, 1977), Vol. 77, p. 11.
- ⁵G. Davies and M. F. Hamer, *Proc. R. Soc. London, Ser. A* **348**, 285 (1976).
- ⁶R. T. Harley, M. J. Henderson, and R. M. Macfarlane, *J. Phys. C* **17**, L233 (1984).
- ⁷N. R. S. Reddy, N. B. Manson, and E. R. Krausz, *J. Lumin* **38**, 46 (1987).
- ⁸K. Holliday, N. B. Manson, M. Glasbeek, and E. Van Oort, *J. Phys. Condens. Matter* **1**, 7093 (1989).
- ⁹D. Redman, S. W. Brown, and S. C. Rand, *J. Opt. Soc. Am. B* **9**, 768 (1992).
- ¹⁰D. A. Redman, S. W. Brown, R. H. Sands, and S. C. Rand, *Phys. Rev. Lett.* **67**, 3420 (1991).
- ¹¹A. T. Collins, *J. Phys. C* **13**, 2641 (1980).
- ¹²W. B. Fowler, *The Physics of Color Centers* (Academic, New York, 1968).
- ¹³N. B. Manson, X.-F. He, and P. T. H. Fisk, *Opt. Lett.* **15**, 1094 (1990).
- ¹⁴A. Leneff and S. C. Rand, following paper, *Phys. Rev. B* **53**, 13 441 (1996).
- ¹⁵A. Abragam and B. Bleaney, *Paramagnetic Resonance of Transition Metal Ions* (Clarendon, Oxford, 1970).
- ¹⁶I. D. Abella, N. A. Kurnit, and S. R. Hartmann, *Phys. Rev.* **141**, 391 (1966); M. Scully, M. J. Stephen, and D. C. Burnham, *ibid.* **171**, 213 (1968); J. P. Gordon, C. H. Wang, C. K. N. Patel, R. E. Slusher, and W. J. Tomlinson, *ibid.* **179**, 294 (1969); D. Grischkowsky and S. R. Hartmann, *Phys. Rev. B* **2**, 60 (1970); J. Schmidt, P. R. Berman, and R. G. Brewer, *Phys. Rev. Lett.* **31**, 1103 (1973).
- ¹⁷M. Sargent III, M. O. Scully, and W. E. Lamb, *Laser Physics* (Addison-Wesley, Reading, Massachusetts, 1974).
- ¹⁸M. B. Walker, *Can. J. Phys.* **46**, 1347 (1968).
- ¹⁹R. M. Chrenko, H. M. Strong, and R. E. Tuft, *Philos. Mag.* **23**, 313(1971).
- ²⁰J. A. Baldwin, *Phys. Rev. Lett.* **10**, 220 (1963).
- ²¹P. Grodzinsky, *Diamond Technology* (N.A.G., London, 1953).
- ²²G. S. Woods and A. T. Collins, *J. Phys. C* **15**, L949 (1982).
- ²³A. T. Collins *et al.*, *J. Phys. D* **20**, 969 (1987).
- ²⁴A. Mainwood, *J. Phys. C* **12**, 2543 (1979).
- ²⁵W. A. Runciman and T. Carter, *Solid State Commun.* **9**, 315 (1971).
- ²⁶G. S. Wood, *Philos. Mag. B* **50**, 673 (1984).
- ²⁷A. T. Collins, M. F. Thomaz, and M. I. B. Jorge, *J. Phys. C* **16**, 2177 (1983).
- ²⁸See, for example, J. Shah, in *Spectroscopy of Semiconductor Microstructures*, edited by G. Fasol, A. Fasolino, and P. Lugli (Plenum, New York, 1989), pp. 535. See, also, S. T. Cundiff and D. G. Steel, *IEEE J. Quantum Electron.* **QE-28**, 2423 (1992).
- ²⁹A. V. Oppenheim and R. W. Schaffer, *Digital Signal Processing* (Prentice-Hall, Englewood Cliffs, NJ, 1975), pp. 242.
- ³⁰E. van Oort, B. van der Kamp, R. Sitters, and M. Glasbeek, *J. Lumin.* **48-49**, 803 (1991).
- ³¹R. Pirc, B. Zeks, and P. Gosar, *J. Phys. Chem. Solids* **27**, 1219 (1966).
- ³²G. Davies, *J. Phys. C* **7**, 3797 (1974).
- ³³F. S. Ham, *Jahn-Teller Effects in Electron Paramagnetic Resonance Spectra* (Plenum, New York, 1969).
- ³⁴S. Saikan, *J. Opt. Soc. Am.* **72**, 514 (1982).